

Sakurai’s Object revisited: new laboratory data for carbonates and melilites suggest the carrier of 6.9 μm excess absorption is a carbonate

J. E. Bowey^{1*} and A. M. Hofmeister²

¹*School of Physics and Astronomy, Cardiff University, Queen’s Buildings, The Parade, Cardiff, CF24 3AA, UK.*

²*Department of Earth and Planetary Sciences, Washington University, 1 Brookings Drive, St. Louis MO 63130, USA.*

Accepted XXX. Received YYY; in original form ZZZ

ABSTRACT

We present new room-temperature 1100–1800 cm^{-1} spectra of melilite silicates and 600–2000 cm^{-1} spectra of three randomly orientated fine-grained carbonates to determine the possible carrier(s) of a 6.9 μm absorption feature observed in a variety of dense astronomical environments including young stellar objects and molecular clouds. We focus on the low-mass post-AGB star Sakurai’s Object which has been forming substantial quantities of carbonaceous dust since an eruptive event in the 1990s. Large melilite grains cannot be responsible for the 6.9 μm absorption feature because the similarly-shaped feature in the laboratory spectrum was produced by very low (0.1 per cent by mass) carbonate contamination which was not detected at other wavelengths. Due to the high bandstrength of the 6.9 μm feature in carbonates, we conclude that carbonates carry the astronomical 6.9 μm feature. Replacement of melilite with carbonates in models of Sakurai’s object improves fits to the 6–7 μm Spitzer spectra without significantly altering other conclusions of Bowey’s previous models except that there is no link between the feature and the abundance of melilite in meteorites. With magnesite (MgCO_3), the abundance of 25- μm -sized SiC grains is increased by 10–50 per cent and better constrained. The mass of carbonate dust is similar to the mass of PAH dust. Existing experiments suggest carbonates are stable below 700 K, however it is difficult to ascertain the applicability of these experiments to astronomical environments and more studies are required.

Key words: methods: laboratory: solid state – stars: AGB and post-AGB –stars: carbon – circumstellar matter – stars: individual – meteorites, meteors, meteoroids

1 INTRODUCTION

A 0.5- μm -wide 6.9 μm absorption feature is of interest in a wide astronomical context because the feature is seen in young stellar objects and molecular clouds which have a complex inventory of dust features due to ices, carbonaceous materials and silicates. The feature also seems to underly narrower PAH absorption in 2005–2008 Spitzer spectra of dust obscuring the carbon-rich born again post-AGB star known as Sakurai’s Object (V4334 Sgr) (Bowey 2021, hereinafter Bo21).

Due to the chemical complexity of YSOs and molecular clouds various carriers have been considered including carbonates although Keane et al. (2001) ruled them out because the laboratory features were too broad. Candidates also include mixtures including methanol ice or another saturated hydrocarbon (Tielens et al. 1984) and mixtures of polycyclic aromatic hydrocarbons (PAHs, Mattioda et al. 2020). Bowey & Hofmeister (2005, hereinafter BH05) noticed that the band seemed to occur in environments with very deep 10 μm silicate absorption bands and found that very high column densities and/or relatively-large (10 μm -sized) crystalline melilite (silicate) grains might be responsible.

Observational constraints were placed on putative band carrier(s)

in a large sample of YSOs and molecular clouds (Boogert et al. 2008, 2011). Keane et al. and Boogert et al. consider the band to have components centred at 6.75 (FWHM~ 0.23 μm) and 6.95 (FWHM~ 0.30 μm) finding the 6.95 μm peak to exist in all environments while the relative 6.75 μm band strength decreases significantly in some YSOs and the changes seem to correlate with the H_2O ice abundance. Boogert et al. (2008) tentatively associated the NH_4^+ ion in UV irradiated ice mixtures with the 6.9 μm feature.

In contrast to these interpretations, carbonates are responsible for 6.9- μm absorption in laboratory spectra of hydrated interplanetary dust particles (IDPs) (e.g. Sandford & Walker 1985) which were assumed to originate from planetesimal and comet environments. Lisse et al. (2007) included carbonates (magnesite (MgCO_3) and siderite (FeCO_3)) in models of freshly produced dust from the deep impact experiment on comet Temple 1 with the caveat that they might be difficult to form in the absence of liquid water. However, apparent difficulties in carbonate formation did not prevent the identification of a far-infrared a band at ~ 90 μm in the spectrum of PN NGC 6302 with calcite (CaCO_3) (e.g. Kemper et al. 2002) but its temperature has to be below 45 K to explain the absence of a 44 μm band (Posch et al. 2007). A 90 μm emission band in YSOs has also been compared with carbonates (e.g. Ceccarelli et al. 2002; Chiavassa et al. 2005). Lisse et al. (2007) described the FIR identifications as problematic

* E-mail: boweyj@cardiff.ac.uk

due to the weakness of the laboratory features and possible confusion with silicate emission bands.

A similar 6.9 μm feature with a companion at 6.3 μm was identified in newly-formed ice-free dust surrounding the currently carbon-rich photosphere of the low mass post-AGB star known as Sakurai's Object (V4334) (Evans et al. 2020, hereinafter Ev20). Once the photosphere was obscured, CN, C₂ and CO were detected in its atmosphere (Eyres et al. 1998). Subsequent infrared observations revealed HCN and C₂H₂ with ¹²C to ¹³C isotope ratios which are consistently lower than typical Solar System values (Ev20). The star is surrounded by a compact 30 × 40 milliarcsec opaque dusty disc or torus inclined at 75 deg to the plane of the sky (Chesneau et al. 2009). It should be easy to decipher the carrier(s) of the 6.9- μm features there since the new dust is theoretically carbon-based. However, beyond the torus the object is surrounded by a faint circular planetary nebula (PN) with a radius of 32 '' which is aligned with the inner torus and there is foreground silicate absorption (Evans et al. 2002).

Bo21 modelled the 6–7- μm bands with a combination of 30 nm-sized PAHs and 20 μm -sized SiC and 10- μm -sized melilite grains. Melilites (oxygen-rich) would not normally be expected in a carbon-rich environment. However, fits to the 8–13.3 μm -range required additional absorption due to submicron-sized *interstellar* silicates, termed astrosilicates, and represented by dust towards Cyg OB2 no. 12. Since the increase in the melilite feature seemed to occur with a decrease in the silicate absorption feature, Bowey proposed that the melilites might be converted from smaller silicate grains in the ancient PN.

Like others, Bo21 used the absence of a formation mechanism to rule carbonates out of consideration in the H₂O-free environment of Sakurai's Object. However, she was unaware that calcium carbonate has been formed under laboratory conditions by exposing amorphous CaSiO₃ (a glass of wollastonite composition) with gaseous CO₂ at pressures > 6 Bar (Day et al. 2013).

A weakness in (BH05) and Bo21 association of melilite with the astronomical 6.9 μm bands is its basis on a single laboratory spectrum and the absence of good laboratory spectra for carbonates in this wavelength range. Therefore we present experimental methods in Section 2, new laboratory spectra of carbonates in Section 3 and more melilites in Sections 4 and 5. Sakurai's Object is modelled with carbonates in Section 6 and revised column densities, torus masses and mass-increase rates are given in Section 7. Mechanisms for astronomical carbonate formation are discussed in Section 8 and the paper is summarised in Section 9.

2 EXPERIMENTAL METHODS

Electron microprobe analysis of the new melilite samples was performed at Washington University using a JEOL-733 equipped with Advance Microbeam automation. The accelerating voltage was 15 kV, beamcurrent was 25 nA, and beam diameter was 10 μm . X-ray matrix corrections were based on a modified Armstrong (1988) CITZAF routine. Silicates and oxides were used as primary standards.

IR absorption spectra were acquired using an evacuated Bomem DA 3.02 Fourier transform spectrometer with an accuracy of ~ 0.01 cm⁻¹ and an SiC source. 1500 scans at 2-cm⁻¹-resolution were obtained with a HgCdTe detector and a KBr beam splitter.

Powders were made by hand-grinding mineral samples to submicron (~ 0.1–1- μm) sizes under alcohol with a pestle in a ceramic mortar and drying them for five minutes. To avoid degrading the crystal structure grinding and drying were limited to 10 and 5 minute

intervals, respectively. Grain size was estimated by the feel of the powder under the pestle; if sizes were too large the grinding procedure was repeated.

Four powder spectra of known and unknown sample thickness were gathered for each mineral. Powders were hand-compressed between two 25 mm-diameter 4 mm-thick KBr discs to make optically-thin films; a reference spectrum of the KBr discs was obtained before applying the sample. Discs were cleaned with lens tissues between runs but some sample can remain in microscopic surface scratches so the discs were reground with 3M polishing plastic with diamond coatings of 9, 5, and 1 μm before taking measurements for a different mineral. A single pair of discs was used for the Carrara marble, magnesite and dolomite samples. Melilite spectra were measured with a different set of discs.

Films of known thickness were measured by compressing powder within apertures between the KBr discs. Apertures were made in the ~ 1.9 μm -thick microphone foils measured by (Bowey, Hofmeister, & Keppel 2020) and with with 6 μm -thick tin gaskets used for IR cells (these were measured with a micrometer). The very thin films required to obtain unsaturated carbonate peaks were obtained by gently squeezing the discs together and rotating them to make a uniform film. Spectra of each sample were taken in the order microphone foil, repeat after squeezing, 6 μm gasket, then take gasket out and run the very thin film. The thinnest calcite film (~ 0.04 μm) is of grains remaining in the scratched KBr discs after cleaning with a lens paper.

Melilite cleavage flakes (chips) were set on an aperture. The unobstructed aperture was used for the reference spectrum. Thicknesses were measured with a micrometer.

2.1 Determination of band strengths and mass absorption coefficients

Laboratory absorbance

$$a = -\log_{10} \frac{I_t}{I_*} = A \times d, \quad (1)$$

where I_t is the intensity of the beam transmitted through the sample and its holder and I_* is the intensity of the beam transmitted through the empty holder. Laboratory absorbance is equivalent to the absorption coefficient, A , times the film thickness d in the spectroscopic, chemical and mineralogical literature. However, astronomers use a natural log absorption coefficient (or optical depth, τ) units, so our data are plotted as

$$\tau(\mu\text{m}^{-1}) = \frac{A}{d} \times 2.3026, \quad (2)$$

where the factor of 2.3026 is derived from the change of base formula.

We present our data as natural log absorption coefficients because this represents attenuation and path length. Mass extinction coefficients, κ (cm²g⁻¹), can be calculated using the relation

$$\kappa = 10^4 \tau / \rho \quad (3)$$

where ρ is the density of the mineral in units of gcm⁻³.

Carbonate spectra of nominally ~ 0.1- μm -thick films were scaled to the height¹ of the ~ 712 cm⁻¹ or 14.0 μm E_⊥c peak because it was unsaturated in all the films and originates from the same orientation as the dominant 1450-cm⁻¹ 6.9- μm peak. ELF routines in the STARLINK DIPSO software package were used to subtract local

¹ Peak areas were not used because reflections contribute to the LO modes and asymmetry in carbonate spectra. For weak modes the LO-TO splitting is low.

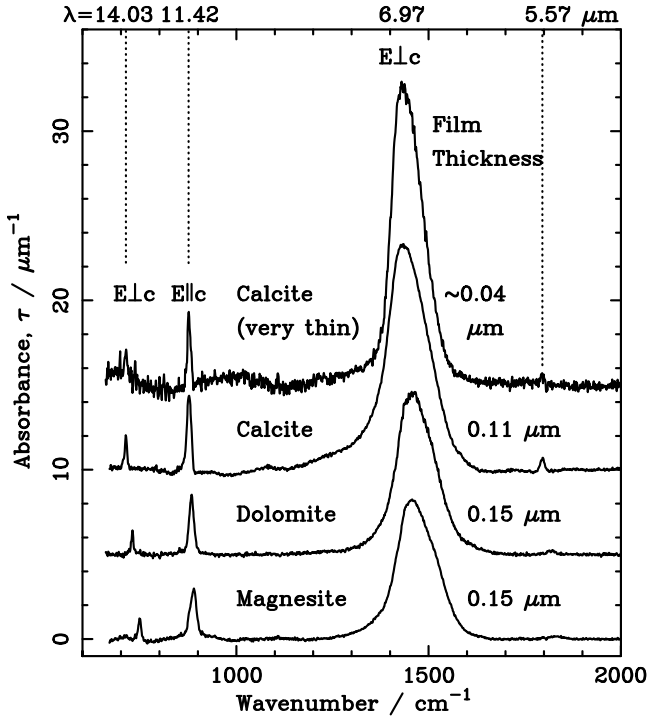


Figure 1. Calibrated carbonate spectra. From bottom to top offsets in y are 0, 5, 10 and 15. Differences in band strengths are intrinsic to the minerals.

baselines and to fit Gaussian peaks. The microphone foils were used as the primary thickness gauge and the $6\ \mu\text{m}$ films for a consistency check. The thickness of the $\sim 0.04\text{-}\mu\text{m}$ film (powder remaining in a scratch on the KBr disc after cleaning) was estimated by matching $712\ \text{cm}^{-1}$ and $876\ \text{cm}^{-1}$ bands to those in the $0.11\ \mu\text{m}$ calcite film. Polynomial baselines were subtracted from the entire spectral range before publication in Figure 1, an unsubtracted spectrum of calcite is shown in Figure 2. Fringe removal was unnecessary.

Local baselines and Gaussian fits to peaks in the powder and chip spectra of melilites Ak₇₀ and Ak₁₃ were obtained with ELF routines. Ak₇₀ overtones were scaled to the height of the $1470\ \text{cm}^{-1}$ ($6.80\ \mu\text{m}$) peak. To ensure the absence of carbonate and other contaminants, the spectrum of, Ak₁₃, was obtained after soaking it in muriatic acid (concentrated HCl) for a few days, drying it, and subtracting the spectrum of an unidentified fluffy residue from the resulting crystals. The baseline subtraction of Ak₇₀ and the subtraction of the spectrum of the residue from the spectrum of Ak₁₃ is described in Appendix A.

3 CARBONATE SPECTRA

We selected marble specimens (e.g. Carrara marble) which are fine grained with randomly orientated crystals, because most infrared carbonate bands depend strongly on crystal orientation (see review by White 1974). Spectra of calcite, CaCO_3 dolomite ($\text{Mg}_{0.5}\text{Fe}_{0.5}\text{CO}_3$) and magnesite (MgCO_3) are presented in Figure 1 and the peaks listed in Table 1. Siderite, FeCO_3 , was not measured because its peak occurs longward of the astronomical band at $\sim 7.03\ \mu\text{m}$ (White 1974). Carbonate spectral features in the $600\text{--}2000\ \text{cm}^{-1}$ -range are due to stretches within the CO_3^{2-} anion and wavelength shifts due to changes in cation are relatively small at $\sim \pm 0.1\ \mu\text{m}$ for the dominant $6.9\text{-}\mu\text{m}$ feature. In calcite, $1434\ \text{cm}^{-1}$ ($6.97\ \mu\text{m}$) and narrow

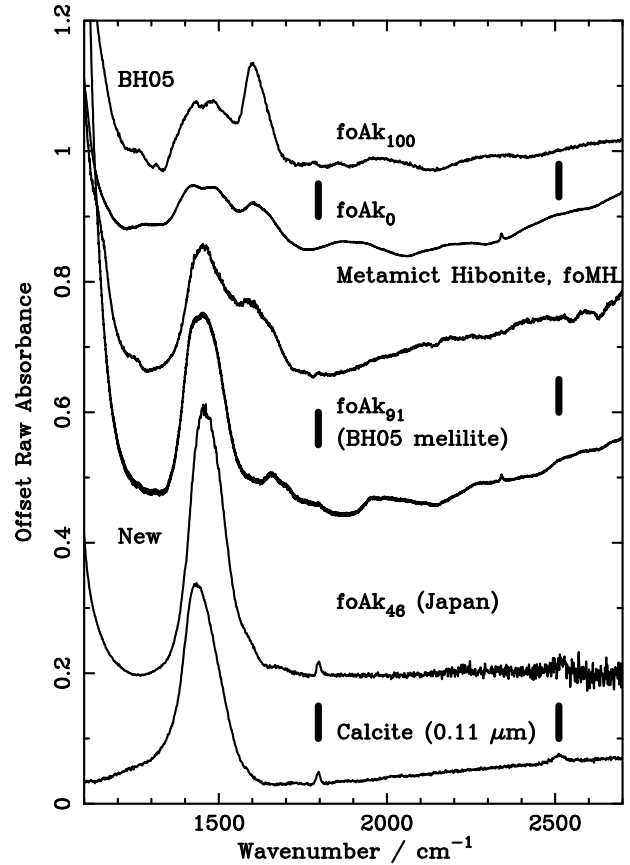


Figure 2. Carbonate contamination in published (BH05) and new melilite (Japan) melilite spectra and calcium carbonate ($0.11\text{-}\mu\text{m}$ -thick Carrara Marble (CaCO_3)) before baseline subtraction. Thick bars indicate the expected position of small carbonate bands.

$713\ \text{cm}^{-1}$ ($14.0\ \mu\text{m}$) peaks are sensitive to $E \perp c$, whilst the $876\ \text{cm}^{-1}$ ($11.4\ \mu\text{m}$) is sensitive to $E \parallel c$. The weak $1796\ \text{cm}^{-1}$ ($5.57\ \mu\text{m}$)-band is a multiphonon mode without an orientational dependence. Band strength estimates are high, $\kappa_{6.9} \sim 27000\text{--}49000\ \text{cm}^2\text{g}^{-1}$ for $\sim 0.1\ \mu\text{m}$ films; differences in band strengths are intrinsic to the minerals.

4 FALSE MELILITE OVERTONE SPECTRA

The melilite group contains paired SiO_4 or $\text{SiO}_4\text{--AlO}_3$ tetrahedra with shared oxygen atoms; the main group ranges from åkermanite $\text{Ca}_2\text{MgSi}_2\text{O}_7$ to gehlenite ($\text{Ca}_2\text{Al}_2\text{SiO}_7$); intermediate melilites have varying combinations of Ca^{2+} , Na^+ , K^+ , Mg^{2+} , Fe^{2+} and Fe^{3+} . Unfortunately carbonate contamination is almost inevitable due to the environments in which melilites are formed. Carbonates and other contaminants are adequately removed by examining the crystals before grinding. Hereinafter, contaminated overtone spectra are distinguished by referring to them as false overtones (fo), foAk_x, where x represents the åkermanite component of the contaminated overtone spectrum. Melilites form from Ca-rich magmas and within thermally metamorphosed carbonate rocks (Deer, Howie & Zussman 1986). Synthetic samples are formed by melting (foAk₁₀₀) or sintering (foAk₀) mixtures of CaCO_3 , $\text{Al}(\text{OH})_3$, MgO and SiO_2 at 1300°C (Charlu, Newton & Kleppa 1981).

Peaks in the $5\text{--}8\text{-}\mu\text{m}$ spectra measured by BH05 are compared

Table 1. Carbonate samples, peaks and estimated band strengths for $\sim 0.1 \mu\text{m}$ powder films.

Sample	Formula	Locality ^a	Peaks μm	ρ^a gcm^{-3}	$\kappa_{6.9}$ cm^2g^{-1}
Calcite	CaCO_3	Carrara, Italy	5.57, 6.97 , 11.42, 14.03	2.72	49000 ^b
Dolomite	$\text{CaMg}(\text{CO}_3)_2$	Eugul, Navarre, Spain	5.50, 6.87 , 11.33, 13.70	2.86	33000
Magnesite ^c	MgCO_3	Brumado, Bahia, Brazil	5.46, 6.87 , 11.25, 13.37	2.98	27000

^a See (Merriman et al. 2018) for sample details.

^b for $0.11\text{-}\mu\text{m}$ film; value for very thin film is ≈ 64000

^c composition from the RRUFF Database <https://rruff.info/> (Lafuente et al. 2015)

Table 2. Spectral characteristics, composition and origins of powdered carbonate-free melilites with well-defined overtone spectra.

Sample	Chemical Formula	Locality ^a	Peaks μm
Ak ₁₃	$(\text{Ca}_{2.02}\text{Na}_{0.07})(\text{Fe}_{0.01}\text{Mg}_{0.15}\text{Al}_{0.83})$ $-(\text{Al}_{0.87}\text{Si}_{1.13})\text{O}_7$	Crestmore, CA USA (Wards)	6.42 6.84
Ak ₇₀ ^b	$\text{Ca}_{1.82}(\text{Fe}_{0.17}\text{Mg}_{0.22}\text{Al}_{0.62})$ $-(\text{Al}_{0.30}\text{Si}_{1.70})\text{O}_7$	Mt Monzani Italy (ExM)	6.39 6.80

^a ExM–Excalibur Mineral Co.

^b composition of $120 \mu\text{m}$ chip

with the spectrum of the $0.11\text{-}\mu\text{m}$ -thick calcite film and an additional melilite sample, foAk₄₆, from Japan (Figure 2) before baseline subtraction. In addition to the prominent 1434 cm^{-1} band, narrow calcite peaks are clearly visible in the Japan sample at 1796 cm^{-1} and 2511 cm^{-1} . Its electron microprobed composition is 94 per cent melilite ($\text{Ca}_{1.94}\text{Na}_{0.07}\text{Fe}_{0.08}\text{Mg}_{0.33}\text{Al}_{0.60}(\text{Al}_{0.54}\text{Si}_{1.46})\text{O}_7$), 5 per cent calcite and 1 per cent iron sulphide. Since silicate overtones for most anhydrous silicates had ($\kappa_{pk} \sim 30\text{--}90$; BH05) it is probable that the higher band strengths of crystalline melilites $\kappa_{pk} \sim 130\text{--}220$ were enhanced by the carbonate impurity.

BH05 and Bo21 found foMH and foAk₉₁ matched astronomical $6.9 \mu\text{m}$ features well. Unfortunately, both spectra have a tiny inflections at 1796 cm^{-1} which are probably the narrow calcite peak. The synthetic end-member åkermanite (Ak₁₀₀) also had a weak peak at 1796 cm^{-1} but there is no hint of this in gehlenite (Ak₀). Other calcite peaks at 876 cm^{-1} and 712 cm^{-1} were invisible due to saturation of the fundamental bands, which is necessary to view the overtones.

In summary, the BH05 overtone spectra with strong $6.9 \mu\text{m}$ features are dominated by the carbonate contamination. BH05 spectra of materials without a $6.9 \mu\text{m}$ band are not contaminated with carbonates. This means that BH05 and Bo21 unknowingly fitted astronomical data with carbonates rather than melilites. The carbonate band is ~ 1000 times stronger than silicate overtones and 5000 times the hibonite overtones, so we suspect the contamination to have been < 1 part in 1000 and otherwise undetectable in the melilite spectra.

5 TRUE MELILITE OVERTONE SPECTRA

Spectra were obtained from $5\text{--}8 \mu\text{m}$ of 7 additional melilites. However the spectra were inconsistent and contained a range of broad bands similar to those in Figure 2. Two samples contained very different bands: an Italian melilite, Ak₇₀, and a gehlenite from Crest-

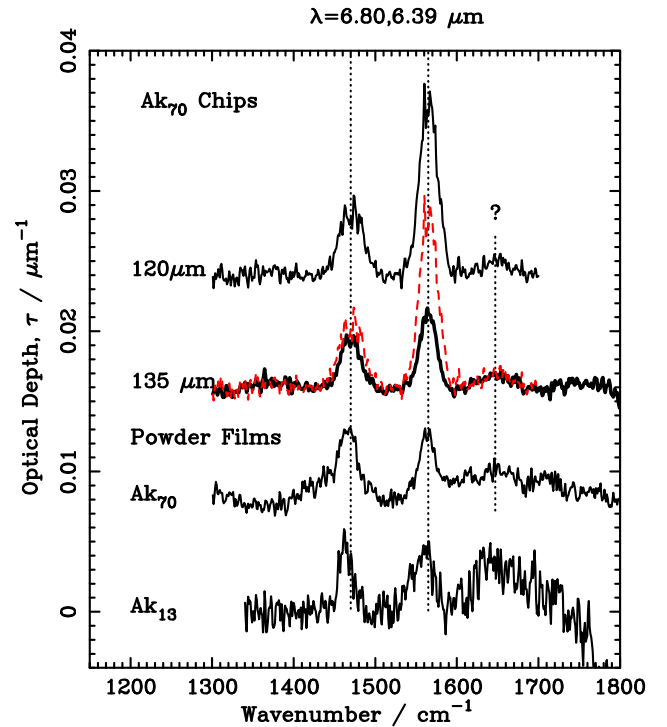


Figure 3. True melilite overtones. The mineral chips show orientational effects. y-axis offsets bottom to top are: 0.000, 0.008, 0.016, 0.024

more, California, Ak₁₃. To ensure the absence of carbonate and other contaminants, the spectrum of, Ak₁₃, was obtained after soaking it in muriatic acid (concentrated HCl) for a few days, drying it, and subtracting the spectrum of a fluffy residue from the resulting crystals. The sample was so small that this provides a consistency check on the shape of the Ak₇₀ overtone spectrum, but is not suitable for data modelling.

The overtone spectra of Ak₇₀ chips and powder films (Figure 3 and Table 2) have two bands centred at 1470 cm^{-1} (FWHM $\sim 29 \text{ cm}^{-1}$), and 1565 cm^{-1} (FWHM $\sim 24 \text{ cm}^{-1}$). The powder peaks are of similar strength ($\kappa_{6.80} \sim 15 \text{ cm}^2\text{g}^{-1}$), but the relative strengths from the chips vary: equal in the $135\text{-}\mu\text{m}$ -thick sample, but in the $120\text{-}\mu\text{m}$ sample the 1565 cm^{-1} peak is twice as strong as the 1470 cm^{-1} peak. We suspect a dependence on crystal orientation with $1565 \text{ cm}^{-1} E \parallel c$ and the other parallel to the a-axis. The extremely weak third peak centred at 1650 cm^{-1} (FWHM ≈ 40) required for baseline determi-

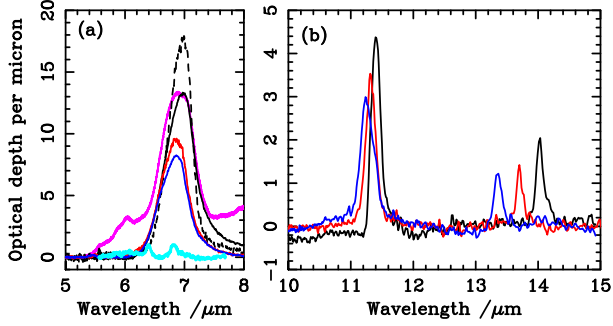


Figure 4. (a) Wavelength comparison of 0.1–0.15- μm -thick calcite (black solid curve), dolomite (red), magnesite (blue) with the BH05 contaminated melilite foAk₉₁ (magenta) and the true melilite overtones, Ak₇₀ (cyan). The black dashed curve denotes the spectrum of the very thin $\sim 0.04 \mu\text{m}$ calcite film. (b) 0.11–0.15 μm -thick carbonate peaks between 10 and 15 μm .

nation might be a H₂O bend from surface sorbed water from the air, an overtone or a combination of the two².

The carbonate spectra are compared with the BH05 melilite and true melilite overtones on a wavelength scale in Figure 4. Although the true melilite overtones might contribute to astronomical 6.9 μm features, their relative weakness makes it unlikely that they would ever be observed.

6 CARBONATE MODELS OF SAKURAI'S OBJECT

True melilite overtones have not been included in these new models of Sakurai's object because they are too narrow and very weak in comparison to the carbonate and PAH bands.

6.1 Models

As in Bo21, the Spitzer 5.9–7.5 μm flux spectra were fitted with an obscured black body model with up to three foreground absorption components. Parameters of the PAH and SiC (or bSiC, where b means big to represent the 25- μm -sized grains) and magnesite components required for the models are listed in Table 3. The flux, F_ν is given by:

$$F_\nu = c_0 B_\nu(T) \exp\left(-\sum_{i=1}^3 c_i \tau_i(\lambda)\right), \quad (4)$$

where $B_\nu(T)$ is the Planck function, and τ_i is the shape of the i^{th} absorption feature, normalised to unity at the tallest peak in the wavelength range of interest, and c_0 and c_1 to c_3 are the fitted scale factors. To determine c_0 , the continuum was matched to the feature at 6.0 μm , i.e. the foreground absorption was assumed zero at this wavelength.

In Bo21 the source flux, F_{ν^*} for fitting the 8.4–13.3 μm spectra was given by,

$$F_{\nu^*} \propto B_\nu(T_1) + B_\nu(T_2) c_{n\text{SiC}} \tau_{n\text{SiC}}(\lambda) \quad (5)$$

where T_1 and T_2 are the temperatures of the optically-thick and

² The four or five evenly-spaced $\tau \lesssim 0.001\text{-}\mu\text{m}^{-1}$ peaks underlying features in the 120 and 130 μm chips might be due to fringing caused by the aperture or crystal-thickness.

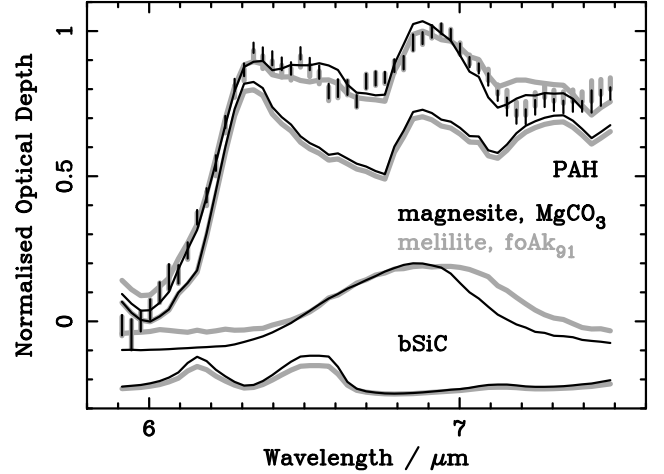


Figure 5. Weighted mean of normalised optical depths obtained with foAk₉₁ melilite in Bo21 (thick grey error bars) and new magnesite (black error bars) with fits and indicated components - thick grey curves denote fits with melilite, black curves denote fits with magnesite. Profiles, fits and fitted components are very similar but the fitted bSiC component is slightly larger with magnesite.

optically-thin emission components and $c_{n\text{SiC}}$ is a scaling constant for normalised emission due to nm-sized SiC grains, $\tau_{n\text{SiC}}(\lambda)$. This emitted continuum was then extinguished by foreground astrosilicate dust to give the observed flux, F_ν ,

$$F_\nu = c'_0 F_{\nu^*} \exp(-c_{pah} \tau_{pah}(\lambda) - c_{sil} \tau_{sil}(\lambda)) \quad (6)$$

where, scaling constant c'_0 , T_2 and c_{sil} were fitted by χ^2 -minimization and c_{pah} was fixed to the value obtained from the 5.9–7.5- μm fits.

The effect of including the carbonate fraction modelled in the 5.9–7.5- μm fits was considered by including it as an additional absorption component.

$$F_\nu = c'_0 F_{\nu^*} \exp(-c_{pah} \tau_{pah}(\lambda) - c_{sil} \tau_{sil}(\lambda) - c_{car} \tau_{car}(\lambda)) \quad (7)$$

where c_{car} was fixed to the value obtained from the 5.9–7.5- μm fits. Continua for merged 5–13.5 μm spectra were derived by setting c_{pah} , c_{sil} and c_{car} , to zero and extending the wavelength range.

6.2 Fits with carbonate change little

All three carbonates provided good fits to the excess 6.9 μm absorption in equation 4. Statistics of the calcite models were similar to those of melilite (foAk₉₁) in Bo21, but fits with dolomite and magnesite were slightly better due to a better match in peak wavelength. Dolomite and magnesite models were statistically indistinguishable from each other ($\Delta\chi^2_\nu \pm 0.00\text{--}0.03$) and variation in c_{pah} , c_{SiC} and c_{mag} and c_{dol} was $\sim \pm 0.01$. Since Mg is estimated to be 12 times more abundant in grains than Ca (Snow & Witt 1996), magnesite was chosen to represent the carbonate in Sakurai's object. Differences in the fitted parameters are due mainly to the nearly symmetrical shape of carbonate bands in comparison to foAk₉₁ which has additional structure and substantial opacity beyond the 6.9- μm band in foAk₉₁ (see Figure 4).

6.2.1 Virtually indistinguishable optical depth profiles

The magnesite optical depth profiles and fit components for each epoch are shown in Figure 6 and listed in Table 4. Revised weighted

Table 3. Laboratory data and band assignments of the C-rich (PAH, bSiC, nSiC and magnesite) and O-rich (foAk₉₁ and astrosilicate) dust components used in the models of Sakurai’s Object; mass absorption coefficients are given at the peak wavelengths marked in bold type; see Bo21 for their derivation. Values for the false melilite, foAk₉₁ used by Bo21 are included for comparison.

Sample	Strongest Band	Approximate Assignment	Size ^a	ρ gcm ⁻³	κ_{pk} 10 ² cm ² g ⁻¹	m_g ^b g	Ref ^c
PAH	6.3	Arom. C=C	53 ₃₀ ⁷⁰ nm	0.39 ^{0.2} _{1.8}	600 ¹²⁰⁰ ₁₃₀ ^d	5.8×10^{-17}	1
bSiC	6.6	Overtone	25 μ m	3.2	2.4	5.0×10^{-8}	2
nSiC	12.3	Si–C stretch	3 nm	3.2	15000	8.6×10^{-20}	2, 3
magnesite	6.87		0.15 μ m	2.98	270	1.0×10^{-14}	
astrosilicate ^e	9.8	Si–O stretch	0.3 μ m	3.3	26	8.9×10^{-14}	
Bo21 false melilite							
foAk ₉₁	6.1, 6.9	Overtone	12 μ m	3.0	2.2	5.2×10^{-9}	

^a Representative grain length assuming approximately cubic geometry.

^b Representative mass of single grain, assuming volume=(size)³

^c Reference for spectrum 1–Carpentier et al. 2012; 2–Hofmeister et al. 2009; 3–Speck, Thompson, & Hofmeister 2005

^d Best estimates. The superscripts and subscripts indicate the range depending on the effective mass density of the soot sample, the value of 1200 pertains to a grain of 30nm and bulk mass density

^e Represented by the line of sight to Cyg OB2 no.12; ρ is an estimate given by the mean of forsterite and enstatite mass densities; κ_{pk} from Bowey & Adamson (2002).

Table 4. Magnesite, MgCO₃, PAH and SiC fits to 5.9–7.5 μ m spectra of Sakurai’s object. The 1 sigma confidence intervals σ , for c_{pah} are 1–2 per cent; for c_{mag} they are normally 5–6 per cent and 8 per cent in Epoch 1. Quantities which vary by more than 10 per cent from those in Bo21 are indicated in bold. Fit quality, χ^2_v and χ^2_{v2} denote three-component and two-component (PAH and melilite only) fits, respectively. $\Delta\chi^2_v$ is the difference between the qualities of the foAk₉₁ and the better magnesite fits. $\tau_{6.3}$ and $\tau_{6.9}$ are the measured optical depths of the 6.3 and 6.9 μ m peaks, respectively.

Ep.	MJD ^a	T/K	c_{pah}	c_{mag}	c_{SiC}	σ	χ^2_v	χ^2_{v2}	$\Delta\chi^2_v$	$\tau_{6.3}$	$\tau_{6.9}$	c_{sil}
1	53475	276	0.080	0.033	0.013	32	0.56	0.62	0.34	0.097	0.10	
2	54225	228	0.12	0.057	0.016	20	0.64	0.86	0.32	0.14	0.15	0.072
3	54388	226	0.15	0.067	0.025	21	0.64	0.83	0.35	0.18	0.19	0.16
4A	54577	224	0.19	0.065	0.028	28	0.52	0.74	0.25	0.23	0.23	0.14
4B	54586	230	0.21	0.059	0.029	14	0.49	0.78	0.030	0.23	0.24	0.12
5	54757	228	0.23	0.075	0.040	13	0.58	0.77	0.12	0.26	0.28	0.11
WM			0.82	0.30	0.13		3.3		1.0	0.94	1.0	

^a Modified Julian Date (MJD) is used to identify the time of the observations. MJD is related to Julian Date (JD) by MJD = JD – 2400000.5

mean optical depth spectrum (black) and components are compared with the Bo21 results (grey) in Figure 5. The revised and original weighted means are virtually indistinguishable despite subtle differences in the fitted components.

6.2.2 Higher and consistent c_{SiC} estimates for different Epochs

Ratioed PAH, magnesite and bSiC optical depths are plotted against their modified julian dates (MJD) in Figure 7; values obtained with foAk₉₁ are indicated in grey. For consistency with Bo21, the fitted optical depths, except c_{SiC} , are ratioed to values obtained with magnesite at Epoch 1; c_{SiC} is ratioed its magnesite value at Epoch 2. The melilite fits plotted in Bo21 are slightly different because those were ratioed to values obtained with melilite.

Fitted optical-depths of the bSiC bands were ~ 10–50 per cent higher than those obtained with foAk₉₁ and the increase in depth was consistent between Epochs. The inferred rate of increase between Epochs 2 and 5 is 1.1 ± 0.4 per year.

6.2.3 Minor changes in c_{pah} and c_{mag}

Values for c_{pah} determined with magnesite were slightly higher at Epochs 4B and 5 giving an average rate of ratioed c_{pah} values 9 per cent higher (0.48 ± 0.01 yr⁻¹); the higher rate of c_{pah} increase during Epochs 2–4B was 8 percent lower (0.91 ± 0.07 yr⁻¹) than with foAk₉₁ due to the lower c_{pah} -value in Epoch 4B. c_{mag} is slightly lower than was c_{mel} ; the rate of increase in c_{mag} is decreased by 20 per cent (0.32 ± 0.04 yr⁻¹) Within the uncertainties these values remain consistent with Ev20’s 0.6 ± 0.2 yr⁻¹ estimate of the rate of increase in dust mass from the emitted flux (λF_λ). Absolute values of \dot{c}_{pah} , \dot{c}_{pah} (Ep2–4B), \dot{c}_{SiC} (Ep2–5) and \dot{c}_{mag} are 0.038 ± 0.01 , 0.073 ± 0.06 , 0.02 ± 0.01 , 0.011 ± 0.001 , respectively, per year.

6.2.4 Negligible changes in 8–13 μ m Fits

Fits of the 8.4–13.3 μ m spectra with revised values of c_{pah} and the original equation 6 component were identical to those in Bo21. New models (equation 7) including a magnesite component produced

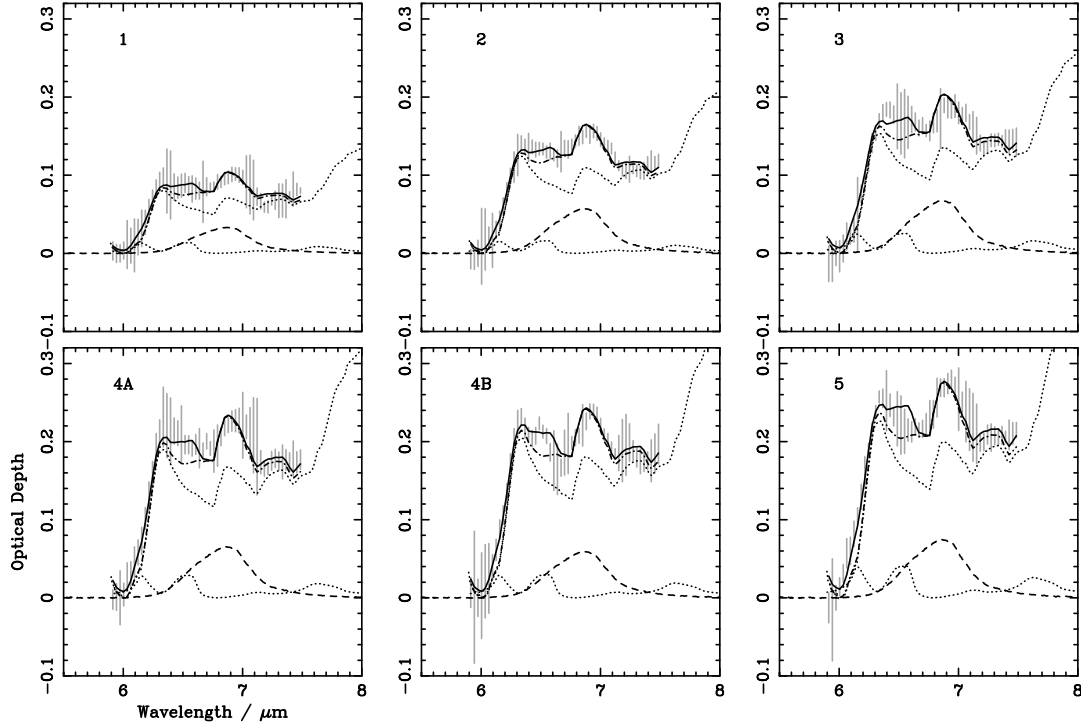


Figure 6. Optical depth profiles of Sakurai's Object (error bars) for the 6–7.5- μm range with fits (solid); fitted PAH (dotted -top), bSiC (dotted) and magnesite (dashed) components. Dot-dash curves indicate the effect of removing the bSiC component from the fits.

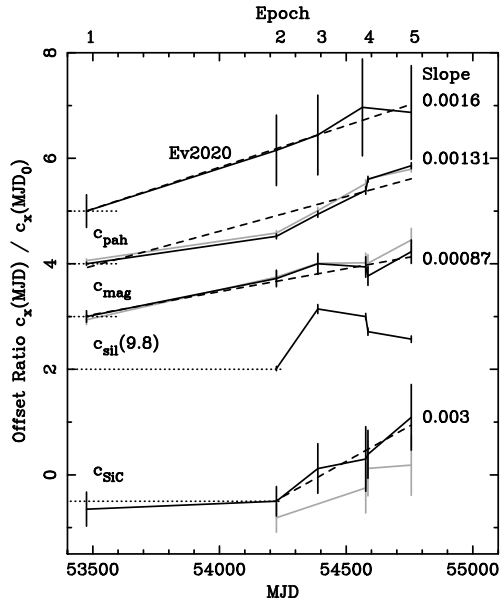


Figure 7. Increases in dust mass during the Spitzer observing period (black) compared with those obtained with melilite by Bo21 (grey). Values obtained by Ev20 are from the flux method. c_{pah} , c_{mag} and c_{SiC} are the fitted optical depths of PAHs and magnesite and bSiC, respectively. Melilite and magnesite indicators, except c_{SiC} , are ratioed to values obtained with magnesite at Epoch 1 (2005-04); c_{SiC} is ratioed to its magnesite value at Epoch 2 (2007-05). Offsets are indicated by dotted lines. Slopes in the figure are in optical depth per day, Uncertainties in the fitted slopes are 0.0005 (Ev20), 0.00004 (c_{pah}), 0.0001 (c_{mag}) and 0.001 (c_{SiC}) per day.

slightly increased absorption at 11.2 μm (Figure 8) which increased the fitted value of c_{sil} by 0–2 per cent, except in Epoch 3 where the increase was 4 per cent. Once again the differences are within the uncertainties even though magnesite (red) might contribute to the 'PAH' feature at 11.3 μm .

Differences in the shape of the modelled optically-thin emission were negligible for the most optically-thin emission features. The relatively unconstrained emission temperatures were 2–15 K warmer than those in Bo21 in Epochs 1, 2, 4A, 4B and 5; Epoch 3, the least optically-thin and least constrained was nominally 82 K warmer.

7 SAKURAI'S OBJECT: REVISED COLUMN DENSITIES AND MASS ESTIMATES

Due to subtle changes in the fitted parameters and very significant changes in the grain properties of the carrier of the broad 6.9- μm band (see Table 3) revised mass density, number density, and dust-mass estimates are required: magnesite grain sizes, absorption coefficients and individual grain masses are respectively, 1.3 per cent, 12000 per cent and 1.9×10^{-4} per cent of those attributed to foAk91. In contrast with the oxygen-rich melilites, which Bo21 assumed to be formed in the external PN, we suggest the carbonaceous magnesite is more likely to be located in the 50 AU compact torus observed by Chesneau et al. (2009) and gain an estimate of its mass.

7.1 Mass and Column Densities

As in Bo21, the mass column density of absorbers, Σ along the line of sight is given by:

$$\Sigma = \rho L = \tau_{pk} / \kappa_{pk}. \quad (8)$$

Table 5. Column Mass Density and Number Density for Dust Absorption Components

Dust Grain Size	Mass Density, Σ $10^{-6} \text{ g cm}^{-2}$			Number Density, n cm^{-2}			Mass of 50 AU torus $10^{-9} M_{\odot}$			Σ $10^{-6} \text{ g cm}^{-2}$	n cm^{-2}	
	PAH	bSiC	magnesite	PAH 53 nm	bSiC 25 μm	magnesite 0.15 μm	PAH	bSiC	magnesite	silicate	silicate 0.3 μm	
Epoch	Date ^a											
1	15-04-2005	1.3 ^{6.1} _{0.67}	54	1.2	2.2×10^{10}	1100	1.2×10^8	1.1	48	1.1	–	–
2	04-05-2007	2.0 ^{9.2} _{1.0}	67	2.1	3.4×10^{10}	1300	2.1×10^8	1.8	59	1.9	27	3.0×10^8
3	15-10-2007	2.5 ¹¹ _{1.2}	104	2.5	4.3×10^{10}	2100	2.5×10^8	2.2	92	2.2	58	6.5×10^8
4A	21-04-2008	3.1 ¹⁴ _{1.6}	116	2.4	5.3×10^{10}	2300	2.4×10^8	2.7	100	2.1	54	6.1×10^8
4B	30-04-2008	3.5 ¹⁶ _{1.7}	123	2.2	6.0×10^{10}	2500	2.2×10^8	3.1	110	1.9	46	5.2×10^8
5	18-10-2008	3.7 ¹⁷ _{1.8}	167	2.8	6.4×10^{10}	3300	2.8×10^8	3.3	150	2.4	42	4.7×10^8
WM ^b		3.3 ¹⁴ _{1.6}	128	2.7	5.7×10^{10}	2600	2.7×10^8				50	5.6×10^8
Rates of increase / yr^{-1}												
Ep. 1–5 ^c		0.64	73	0.39	1.1×10^{10}	1500	0.39×10^8	0.56	65	0.34		
Ep. 2–4B		1.2			2.1×10^{10}			1.1				

^a day-month-year

^b PAH, bSiC and melilite -from fits to weighted mean spectrum scaled to mean of Epochs 3–5 ($\tau_{6,9} \approx 0.24$); nSiC and astrosilicate from mean of Epochs 3–5.

^c Italicised values for bSiC are based on Ep 2–5

and the column number density of grains, n , is obtained by dividing Σ , by the single-grain masses, m_g , in Table 3. We assume that the cold PAHs and bSiC grains are located in a cylindrical volume of radius, $R = 50$ AU and height of 50 AU and that Sakurai’s object is at a distance of 3.5kpc so that

$$M_{50AU} \approx 8.8 \times 10^{-4} \Sigma M_{\odot} \quad (9)$$

and the rate of mass increase can be deduced by replacing Σ with $\dot{\Sigma}$.

Rates of mass increase are determined by multiplying the gradients of the increases by the fitted constants c_{pah} , c_{mag} at Epoch 1, or Epoch 2 (c_{SiC}) in Figure 7 as appropriate³.

Values of Σ , n and torus-mass for each carbonaceous dust component and are listed in Table 5: values for PAHs and bSiC are revised, the magnesite components are new, and the foreground silicate column densities are unchanged. Rates of increase, $\dot{\Sigma}$, \dot{n} , and \dot{M}_{50AU} in the carbonaceous components are listed below the main table.

7.2 Rates of increase

The rate of increase in PAH mass-density, $\dot{\Sigma}_{pah} = 0.64 \times 10^{-6} \text{ g cm}^{-2}$ in Epochs 1–5, is 3 per cent higher with magnesite than with foAk₉₁; with magnesite the enhanced rate between Epochs 2–4B is twice the average rate for Epochs 1–5 at $1.2 \times 10^{-6} \text{ g cm}^{-2} \text{ yr}^{-1}$, but 14 per cent lower than obtained with foAk₉₁. This gives n_{pah} increase rates of 1.1 to $2.1 \times 10^{10} \text{ grains cm}^{-2} \text{ yr}^{-1}$ and an increase in the torus mass of $0.56 - 1.1 \times 10^{-9} M_{\odot} \text{ yr}^{-1}$. The enhanced rate is 10 times lower than Evans estimate for May 1999 (11×10^{-9}) based on a different set

of assumptions but the increased rate probably still correlates with the period of enhanced mass loss identified by Evans et al. (2020) and Tyne et al. (2002) who estimated a 3.6 ratio in mass-loss rate between May 1999 and September 2001.

For bSiC, $\dot{\Sigma}_{SiC} = 73 \times 10^{-6} \text{ g cm}^{-2} \text{ yr}^{-1}$ or $1500 \text{ grains cm}^{-2} \text{ yr}^{-1}$; the mass increase rate is $65 \times 10^{-9} M_{\odot} \text{ yr}^{-1}$ between Epochs 2 and 5. For magnesite, the mean rate of mass density increase is $\dot{\Sigma}_{mag} = 0.39 \times 10^{-6} \text{ g cm}^{-2} \text{ yr}^{-1}$ or $3.9 \times 10^7 \text{ grains cm}^{-2} \text{ yr}^{-1}$; if carbonates are located in the torus the mass increase rate is $0.34 \times 10^{-9} M_{\odot} \text{ yr}^{-1}$.

7.3 Results

These models replace fits with large melilite grains in Bo21 for fits with submicron-sized carbonate grains. The modelled PAH column densities and torus masses for each Epoch are the same to within ± 10 per cent; the fitted component of large SiC grains (bSiC) is better constrained and 10–50 per cent higher. Astrosilicate column densities are unchanged. These results are not sufficiently altered to affect Bo21’s conclusions about the formation time of the PAHs or bSiC, but the link between astrosilicate coagulation to melilites is removed as is the connection between these observations and the abundance of melilite in meteorites.

Due to differences in formation rate, carbonate (magnesite) mass densities and torus masses are similar to the those inferred for PAHs for Epochs 1–3, but lower for Epochs 4A–5. Ratios of particle number density for silicates and magnesite vary between 1.4 (Epoch 2) to 2.5 (Epochs 3–4B) to 1.7 (Epoch 5). The ratio of PAH to magnesite particles is 170 (Epochs 1–3), to 230 (Epoch 4A–5). The ratio of PAH to SiC number density is $\sim 2.3 \times 10^7$.

³ Bo21 did not remember to multiply the gradients by Table 4 at Epoch 1 before quoting them, to correct this use the values for Epoch 1 in her Table 3, namely $c_{pah} = 0.085$ and $c_{mel} = 0.031$

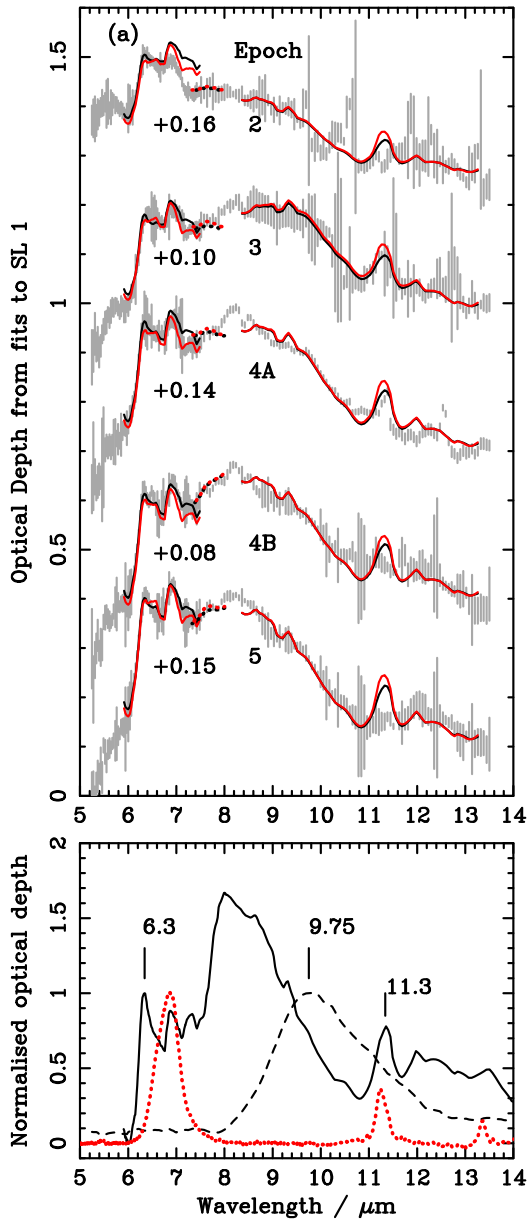


Figure 8. Optical depth profiles (grey error bars) obtained with modelled 8.3–13.3 μm continua; offsets in the Y-axis are 0.0, 0.3, 0.6, 0.9 and 1.2; 8–13 μm solid curves are the fitted absorption features obtained with magnesite (red) and melilite (black), 6–7.5 μm are the fitted features from the SL 2 offset in the Y-axis to match the level of the longer-wavelength fits (additional offsets are indicated); dotted curves between 7.5 and 8.0 μm indicate the contribution from bSiC extrapolated from the magnesite (red) and melilite (black) SL 2 fits. Magnesite (red dotted) with the other absorption profiles used to model 8.3–13.3 μm spectra: PAH spectrum (solid) and silicate absorption (dashed) modelled with the profile of interstellar dust towards Cyg OB2 no. 12. Modelling profiles are normalised at 6.3 and 9.75 μm , respectively. Magnesite is normalised at 6.9 μm .

8 HOW ARE ASTRONOMICAL CARBONATES FORMED?

During the period of the observations, the column density of magnesite in Sakurai’s Object increased at a rate of $0.39 \times 10^{-6} \text{gcm}^{-2} \text{yr}^{-1}$, about 0.6 of the average rate of increase in PAH mass (Section 7.2). Therefore it seems that carbonates are either condensing directly from gas, or other dust components are being converted

to carbonates. The experiments discussed below suggest carbonates condense from gas below 700 K and decompose above about 730 K. The inferred carbonates in Sakurai’s Object appear as absorption features in dust which is cooler than the 280–230 K continuum used in modelling the absorption features (see models in Section 6.1).

8.1 Direct condensation from the gas is problematic

Direct condensation from the gas is problematic because chemical equilibrium and non-equilibrium models suggest <1 per cent of the dust condensed from gases outflowing from oxygen-rich AGB stars could be CaCO_3 (or another carbonate Ferrarotti & Gail 2005) and that the amount formed in a carbon-rich envelope like that of Sakurai’s Object will be ≈ 0 due to the absence of free oxygen. Analogous laboratory experiments might be chemical vapour deposition in a CO-rich or CO_2 -rich and oxygen- and H_2O -poor atmosphere. We have found none for a CO atmosphere. The nearest we can find are:

(i) an experiment by Sulimai et al. (2021) who formed thin films of calcium carbonate on FTO (fluorine-doped tin) glass substrates by chemical vapour deposition (CVD) from heated CaCl_2 solution and CO_2 gas at a flow rate of 100 standard cubic centimetres per minute at 1 bar. CaCO_3 formed at temperatures of 623–723 K with a peak formation rate at 673 K.

(ii) Unidentified carbonate contamination in the infrared spectra of vapour-condensed CaO and $\text{Ca}(\text{OH})_2$ smokes published by Kimura & Nuth (2005). In these experiments Ca metal was placed in a graphite boat inside an alumina furnace tube and exposed to a hydrogen-rich atmosphere at 0.1 bar and temperatures between 1080 and 1170 K. Spectra of their run products are similar to our carbonate spectra with characteristic narrow peaks near 11.4 and 14.0 μm as well as the band at 6.9 μm . We conclude that the disordered sample picked up CO_2 during the experiment or from the air⁴ as well as the discussed water to form a surface layer of carbonate before their spectra were obtained. The main 31- μm peak in CaO has a shoulder at 17.9 μm (Hofmeister, Keppel & Speck 2003) which appears in the Kimura & Nuth (2005) data which extend to 25 μm .

8.2 Formation from older dust

Does the small reduction in the optical depth of the foreground silicate feature indicate that silicates are being converted to carbonates? Day et al. (2013) have formed metastable calcium carbonate (vaterite and calcite) by exposing room-temperature amorphous CaSiO_3 glass in a sapphire high-pressure tube to gaseous CO_2 at a pressure of 6 bar - well above ambient astronomical pressures. Their carbonate is stable at temperatures below 753 K; above this it starts to anneal and break down into CaSiO_3 and CO_2 . Sulimai et al. (2021) also showed that CaCO_3 decomposes between 723 K and 873 K. If carbonates also fit the broad 6.9- μm band in YSOs and molecular clouds it seems likely that exposure of pre-existing grains to CO_2 and water might also result in carbonate formation but appropriate experiments are required to prove this.

⁴ The infrared carbonate bands are known to appear rapidly when CaO is obtained by burning limestone (CaCO_3) in air (Galván-Ruiz et al. 2009)

9 SUMMARY

We present new 600–2000 cm^{-1} room-temperature spectra of 3 carbonates: calcite, dolomite and magnesite which have strong broad peaks centred at 6.97, 6.87 and 6.87 μm , respectively. These peaks resemble an astronomical absorption feature observed in a variety of dense astronomical environments including young stellar objects and molecular clouds. We focus on fitting spectra of low-mass post-AGB star Sakurai's Object which has been forming substantial quantities of carbonaceous dust since an eruptive event in the 1990s.

Comparison of published melilite-group and hibonite overtone spectra obtained by [Bowey & Hofmeister \(2005\)](#) with our carbonate spectra shows that they are dominated by features due to previously unrecognised carbonate contamination. Thus [Bowey & Hofmeister \(2005\)](#) and [Bo21](#) were fitting the astronomical data with bands due to carbonates.

New overtone spectra obtained from uncontaminated melilite samples contain two $\sim 0.1 \mu\text{m}$ -wide peaks centred at 6.4 and 6.8 μm ; the mass absorption coefficient of the 6.8 μm peak is $\lesssim 0.05$ per cent of the value for carbonates. These bands are too narrow and too weak to provide a measurable contribution to the feature in Sakurai's Object and would probably not contribute to other features either. This removes the proposed links between melilites in Sakurai's Object and the abundance of melilite in meteorites.

Replacement of melilite with magnesite or dolomite in models of Sakurai's Object produces statistically better fits to the 6–7.5- μm Spitzer spectra without significantly altering other conclusions of Bowey's previous models. The main difference is a 10–50 per cent-larger component due to 25 μm -sized SiC grains which increases consistently between epochs. If the carbonates contribute to the mass of the 50 AU torus, the mass is similar to the mass of PAH dust between 2005 April and 2007 October, but lower between 2008 April and 2008 October. On average PAH particles are 2.3×10^7 more abundant than SiC grains and 200 times more abundant than magnesite grains, based on their respective particle sizes of 53nm, 25 μm and 0.15 μm .

Experimental evidence relevant to carbonate formation in low pressure astronomical environments is scarce, although carbonates appear to be stable at temperatures below about 700 K. Evaluating a feasible mechanism is thus challenging. Direct condensation from outflowing gas has been invoked for many species. Alternatively, silicates are being converted to carbonates or they are being made by other chemical changes in pre-existing dust. The small reduction in the optical depth of the foreground silicate feature might indicate that silicates are being converted to carbonates.

ACKNOWLEDGEMENTS

We thank the reviewer, Joseph Nuth, for a positive and helpful report. JEB and the purchase of samples for the experiments were funded by a 2-yr Science and Technology Research Council Ernest Rutherford Returner Fellowship (ST/S004106/1) plus a 6 month extension from Cardiff University. AMH was supported by the USA National Science Foundation. We thank Paul Carpenter of Washington University for the microprobe analyses. LR Spitzer spectra were obtained from the Combined Atlas of Sources with Spitzer/IRS Spectra (CASSIS), a product of the Infrared Science Center at Cornell University, supported by NASA and JPL. Observations were made with the Spitzer Space Telescope, which was operated by the Jet Propulsion Laboratory, California Institute of Technology under a contract with NASA.

DATA AVAILABILITY

The carbonate and true melilite overtone spectra presented in this article are subject to a partial embargo of 12 months from the publication date of the article during which the data will be available from the authors by request. Once the embargo expires the data will be available from <https://zenodo.org/communities/mineralspectra/>

REFERENCES

- Armstrong J., 1988, in Newbury D. E., ed., *Microbeam Analysis*. San Francisco Press, San Francisco, p. 469
- Boogert A. C. A., Pontoppidan K. M., Knez C., Lahuis F., Kessler-Silacci J., van Dishoeck E. F., Blake G. A., et al., 2008, *ApJ*, 678, 985. doi:10.1086/533425
- Boogert A. C. A., Huard T. L., Cook A. M., Chiar J. E., Knez C., Decin L., Blake G. A., et al., 2011, *ApJ*, 729, 92. doi:10.1088/0004-637X/729/2/92
- Bowey J. E., 2021, *MNRAS*, 505, 568. doi:10.1093/mnras/stab1305
- Bowey J. E., Hofmeister A. M., Keppel E., 2020, *MNRAS*, 497, 3658. doi:10.1093/mnras/staa2227
- Bowey, J. E., Hofmeister, A. M. 2005, *MNRAS*, 358, 1383
- Bowey, J. E., Adamson A. J. 2002, *MNRAS*, 334, 94
- Carpentier Y., Féraud G., Dartois E., Brunetto R., Charon E., Cao A.-T., d'Hendecourt L., et al., 2012, *A&A*, 548, A40. doi:10.1051/0004-6361/201118700
- Ceccarelli C., Caux E., Tielens A. G. G. M., Kemper F., Waters L. B. F. M., Phillips T., 2002, *A&A*, 395, L29. doi:10.1051/0004-6361:20021490
- Chang, L.L.Y., Howie, R.A., Zussman J. 1996 *Non-silicates: Sulphates, carbonates, phosphides, halides*. Longman Group Limited, Essex U.K.
- Charlu T. V., Newton R. C., Kleppa O. J., 1981, *Geochim. Cosmochim. Acta*, 45, 1609
- Chesneau O., Clayton G. C., Lykou F., De Marco O., Hummel C. A., Kerber F., Lagadec E., et al., 2009, *A&A*, 493, L17. doi:10.1051/0004-6361:200811173
- Chiavassa A., Ceccarelli C., Tielens A. G. G. M., Caux E., Maret S., 2005, *A&A*, 432, 547. doi:10.1051/0004-6361:20041891
- Day S. J., Thompson S. P., Parker J. E., Evans A., 2013, *A&A*, 553, A68. doi:10.1051/0004-6361/201321138
- Deer, W. A., Howie, R. A., Zussman, J. *Rock-forming minerals*, Vol 1B *Disilicates and Ring Silicates*, 2nd Ed, London : Longman 1986
- Duerbeck H. W., Benetti S., 1996, *ApJL*, 468, L111. doi:10.1086/310241
- Evans A., Gehrz R. D., Woodward C. E., Banerjee D. P. K., Geballe T. R., Clayton G. C., Sarre P. J., et al., 2020, *MNRAS*, 493, 1277. doi:10.1093/mnras/staa343
- Evans A., Geballe T. R., Smalley B., Tyne V. H., Eyres S. P. S., 2002, *A&A*, 394, 971. doi:10.1051/0004-6361:20021229
- Eyres S. P. S., Evans A., Geballe T. R., Salama A., Smalley B., 1998, *MNRAS*, 298, L37. doi:10.1046/j.1365-8711.1998.01898.x
- Ferrarotti A. S., Gail H.-P., 2005, *A&A*, 430, 959. doi:10.1051/0004-6361:20041856
- Galván-Ruiz M., Hernández, J., Baños L., Noriega-Montes J., Rodríguez-García M. E. 2009 *Journal of Materials in Civil Engineering*, 21, 694, DOI: 10.1061/(ASCE)0899-1561(2009)21:11(694)
- Geballe T. R., Evans A., Smalley B., Tyne V. H., Eyres S. P. S., 2002, *Ap&SS*, 279, 39
- Helling C., Jorgensen U. G., Plez B., Johnson H. R., 1996, *A&A*, 315, 194
- Hinkle K. H., Joyce R. R., 2014, *ApJ*, 785, 146. doi:10.1088/0004-637X/785/2/146
- Hinkle K. H., Joyce R. R., Matheson T., Lacy J. H., Richter M. J., 2020, *ApJ*, 904, 34. doi:10.3847/1538-4357/abbd9a
- Hofmeister A. M., Pitman K. M., Goncharov A. F., Speck A. K., 2009, *ApJ*, 696, 1502. doi:10.1088/0004-637X/696/2/1502
- Hofmeister, A. M., Keppel, E., Speck, A. K., 2003, *MNRAS*, 345, 16
- Keane J. V., Tielens A. G. G. M., Boogert A. C. A., Schutte W. A., Whittet D. C. B., 2001, *A&A*, 376, 254. doi:10.1051/0004-6361:20010936
- Kemper F., Jäger C., Waters L. B. F. M., Henning T., Molster F. J., Barlow M. J., Lim T., et al., 2002, *Natur*, 415, 295. doi:10.1038/415295a

- Kimura Y., Nuth J. A., 2005, *ApJ*, 630, 637. doi:10.1086/431965
- Lisse C. M., Kraemer K. E., Nuth J. A., Li A., Joswiak D., 2007, *Icar*, 187, 69. doi:10.1016/j.icarus.2006.11.019
- Lafuente B., Downs R T, Yang H, Stone N (2015) The power of databases: the RRUFF project. In: *Highlights in Mineralogical Crystallography*, T Armbruster and R M Danisi, eds. Berlin, Germany, W. De Gruyter, pp 1-30.
- Mattioda A. L., Hudgins D. M., Boersma C., Bauschlicher C. W., Ricca A., Cami J., Peeters E., et al., 2020, *ApJS*, 251, 22. doi:10.3847/1538-4365/abc2c8
- Merriman J. D., Hofmeister A. M., Roy D. J., Whittington A. G., 2018, *Geosp*, 14, 1961. doi:10.1130/GES01581.1
- Nakano S., Sakurai Y., Hazen M., McNaught R. H., Benetti S., Duerbeck H. W., Cappellaro E., et al., 1996, *IAUC*, 6322
- Pollacco D., 1999, *MNRAS*, 304, 127. doi:10.1046/j.1365-8711.1999.02300.x
- Posch T., Baier A., Mutschke H., Henning T., 2007, *ApJ*, 668, 993. doi:10.1086/521390
- Sandford, S. A., Walker, R. M. 1985, *ApJ*, 291, 838
- Snow T. P., Witt A. N., 1996, *ApJL*, 468, L65. doi:10.1086/310225
- Speck A. K., Thompson G. D., Hofmeister A. M., 2005, *ApJ*, 634, 426. doi:10.1086/496955
- Sulimai, N. H., Salifairus, M. J., Khusaimi, Z. et al. *J Mater Sci: Mater Electron* 32, 3072. doi:10.1007/s10854-020-05057-0
- Tielens A. G. G. M., Allamandola L. J., Bregman J., Goebel J., D'Hendecourt L., Witteborn F. C., 1984, *ApJ*, 287, 697. doi:10.1086/162728
- Tyne V. H., Evans A., Geballe T. R., Eyres S. P. S., Smalley B., Duerbeck H. W., 2002, *MNRAS*, 334, 875. doi:10.1046/j.1365-8711.2002.05561.x
- White, W. B., Ch 12 in "The Infrared Spectra of Minerals", Mineralogical Society of Great Britain and Ireland 1974:01,doi:10.1180/mono-4.12 page 227.

APPENDIX A: CORRECTION OF AK₇₀ AND AK₁₃ SPECTRA

Local baselines were subtracted from the spectra of the Ak₇₀ chips and powder film (Figure A1(a)) by fitting three peaks at 1466, 1563 and 1647 cm⁻¹. The chip spectra also exhibited a broad peak at 1800 cm⁻¹ which might be due to H₂O inclusions in the crystal. There is no hint of carbonate contamination in this spectrum or in Ak₁₃ because the broad 1432 cm⁻¹ peak and the narrow peaks are absent.

The Ak₁₃ spectrum was obtained from crystals embedded in an unknown fluffy residue with a peak at ~ 1630cm⁻¹ (Figure A1 (b)). Baselines were subtracted from the contaminated spectrum and the fluff spectrum. The fluff spectrum was removed by subtracting its scaled peak from the contaminated Ak₁₃ spectrum. The result (red) was then fitted with a 2nd order polynomial and three Gaussian peaks between 1340 and 1750 cm⁻¹. The polynomial was subtracted to produce the spectrum in Figure 3.

This paper has been typeset from a $\text{\TeX}/\text{\LaTeX}$ file prepared by the author.

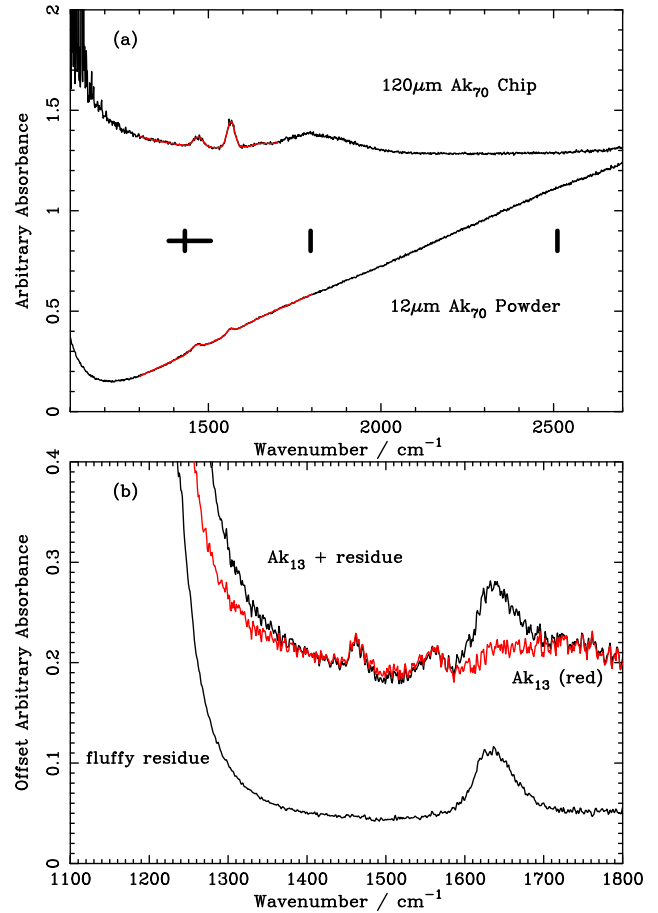


Figure A1. (a) Comparison between spectra of a melilite Ak₇₀ chip and the powdered mineral before baseline removal. Spectra are shown with the fitted baselines and Gaussian peaks (red). Vertical bars indicate the likely positions of narrow bands due to carbonate contamination, the crossed bar indicates the FWHM of the broadest carbonate peak centred near 1432 cm⁻¹. There is no carbonate contamination in this sample. (b) Subtraction of feature due to the unidentified fluffy residue with the Ak₁₃ crystals.